

Key Points:

- An empirical equatorial pitch angle distribution model of 1–50 keV electrons is constructed based on the Van Allen Probes observations
- The anisotropy of 1–50 keV electrons strongly enhances during active times, suggesting their critical role in generating chorus waves
- Energy-dependent patterns of enhanced anisotropy region of 1–50 keV electrons during active times are found

Correspondence to:

H. Zhao,
zzh0054@auburn.edu

Citation:

Zhao, H., Friedel, R. H. W., Chen, Y., Baker, D. N., Li, X., Malaspina, D. M., et al. (2021). Equatorial pitch angle distributions of 1–50 keV electrons in Earth's inner magnetosphere: An empirical model based on the Van Allen Probes observations. *Journal of Geophysical Research: Space Physics*, 126, e2020JA028322. <https://doi.org/10.1029/2020JA028322>

Received 7 JUN 2020
Accepted 29 NOV 2020

Equatorial Pitch Angle Distributions of 1–50 keV Electrons in Earth's Inner Magnetosphere: An Empirical Model Based on the Van Allen Probes Observations

H. Zhao^{1,2} , R. H. W. Friedel³ , Y. Chen³ , D. N. Baker¹ , X. Li¹ , D. M. Malaspina¹ , B. A. Larsen^{3,4} , R. M. Skoug³ , H. O. Funsten³ , G. D. Reeves^{3,4}, and A. J. Boyd⁵ 

¹LASP, University of Colorado Boulder, Boulder, CO, USA, ²Department of Physics, Auburn University, Auburn, AL, USA, ³LANL, Los Alamos, NM, USA, ⁴The New Mexico Consortium, Los Alamos, NM, USA, ⁵Aerospace Corporation, Chantilly, VA, USA

Abstract Using 7 years of data from the Helium, Oxygen, Proton, and Electron instrument on the Van Allen Probes, equatorial pitch angle distributions (PADs) of 1–50 keV electrons in Earth's inner magnetosphere are investigated statistically. An empirical model of electron equatorial PADs as a function of radial distance, magnetic local time, geomagnetic activity, and electron energy is constructed using the method of Legendre polynomial fitting. Model results show that most equatorial PADs of 1–10s of keV electrons in Earth's inner magnetosphere are pancake PADs, and the lack of butterfly PADs is likely due to their relatively flat or positive flux radial gradients at higher altitudes. During geomagnetically quiet times, more anisotropic distributions of 1–10s of keV electrons at dayside than nightside are observed, which could be responsible for moderate chorus wave activities at dayside during quiet times as reported by previous studies. During active times, the anisotropy of 1–10s of keV electrons significantly enhances, consistent with the enhanced chorus wave activity during active times and suggesting the critical role of 1–10s of keV electrons in generating chorus waves in Earth's inner magnetosphere. Different enhanced anisotropy patterns of different energy electrons are also observed during active times: at $R > \sim 4 R_E$, keV electrons are more anisotropic at dawn to noon, while 10s of keV electrons have larger anisotropy at midnight to dawn. These differences, combined with the statistical distribution of chorus waves shown in previous studies, suggest the differential roles of electrons with different energies in generating chorus waves with different properties.

1. Introduction

As one of the most important characteristics of energetic charged particles in Earth's inner magnetosphere, pitch angle distribution (PAD) carries essential information on physical processes and their effects on charged particles. Created by the pitch angle (PA)-dependent effects of various source and loss processes, electron PADs can help identify the existence of specific physical mechanisms. Due to their importance, the PADs of relativistic electrons have been widely studied (e.g., Chen, Friedel, et al., 2014; Chen, Reeves, et al., 2014; Gannon et al., 2007; Shi et al., 2016; West et al., 1973; Zhao et al., 2014a, 2014b, 2018). Three major types of PADs of relativistic electrons have been recognized in Earth's inner magnetosphere: pancake, flattop, and butterfly (e.g., West et al., 1973; Zhao et al., 2018). Figure 1 shows examples of three major types of PADs. The pancake PAD has flux peaking at 90° PA and gradually decreasing as PA gets smaller (Figure 1a). The butterfly PAD has flux peaking at some intermediate PA with lower fluxes at higher and lower PAs (Figure 1c). The flattop PAD is a combination of the two: the particle flux is relatively constant at a wide PA range centered around 90° PA (Figure 1b).

The spatial distribution and formation of three major types of PADs of relativistic electrons have been extensively studied. The pancake PADs are generally located at dayside (e.g., West et al., 1973). They are believed to form as a result of the diffusive loss of particles to the atmosphere, while inward radial diffusion also contributes to the formation of pancake PADs by increasing the particle's momentum component that perpendicular to the local magnetic field more significantly than the parallel component (e.g., Schulz & Lanzerotti, 1974). The butterfly PADs often dominate at nightside at larger L-shells (e.g., Ni et al., 2016; West et al., 1973; Zhao et al., 2018). They form mainly because of drift shell splitting and magnetopause shadowing and/or negative radial flux gradient (e.g., Selesnick & Blake, 2002). Some studies also pointed out that

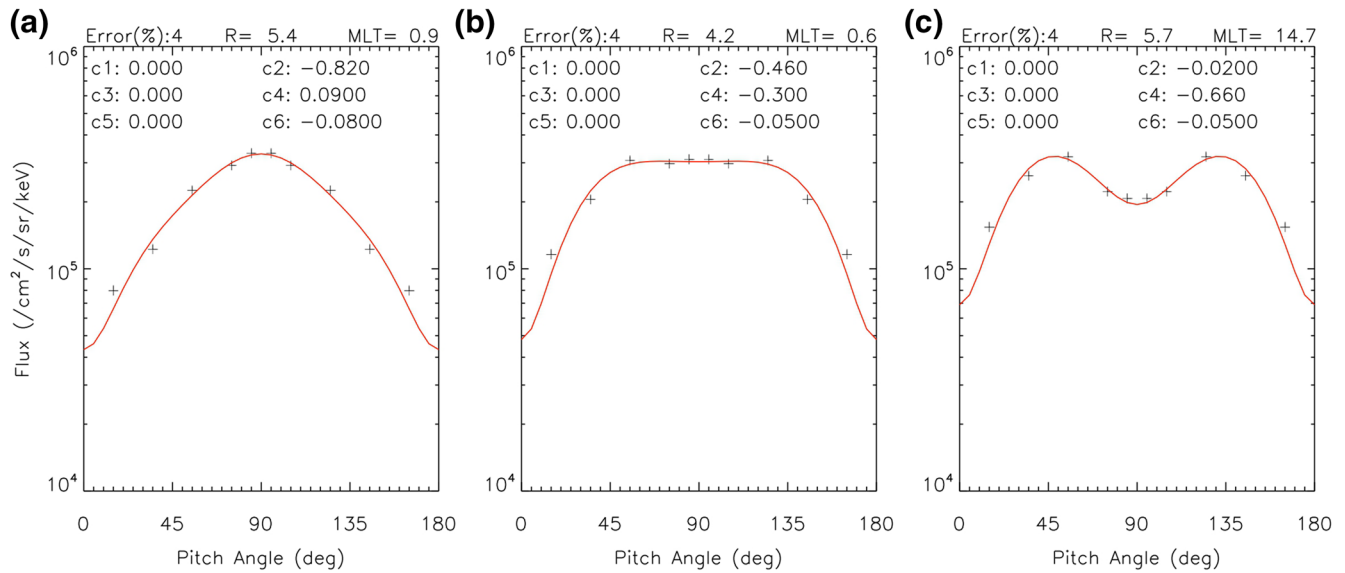


Figure 1. Examples of (a) pancake, (b) flattop, and (c) butterfly pitch angle distributions. Black crosses show flux data of ~ 30 keV electrons from the HOPE instrument on the Van Allen Probe—A (propagated to the magnetic equator and averaged in 5 min assuming symmetric PADs around 90° PA), and red curves show the Legendre polynomial fitting results. The coefficients of Legendre polynomials are shown in each panel. HOPE, Helium, Oxygen, Proton, and Electron; PAD, pitch angle distribution.

the butterfly PADs could be caused by local heating by whistler-mode chorus waves that is more effective for off-equator electrons (e.g., Horne et al., 2005), or scattering of near-equatorially mirroring electrons by magnetosonic waves (e.g., J. Li et al., 2016; W. Li et al., 2016). The flattop PADs can be a transition between the pancake and the butterfly PADs, and they could also be caused by strong wave-particle interactions (e.g., Horne et al., 2003). They are often present near dawn and dusk at a higher L region (e.g., Zhao et al., 2018).

Although the PADs of relativistic electrons in the radiation belts have been intensively studied, the statistical distribution and characteristics of ~ 1 – 10 s of keV electron equatorial PADs received limited attention mainly due to insufficient observations. Understanding 1–10s of keV electron PADs will not only provide a more comprehensive picture of energetic electron distributions in Earth's inner magnetosphere, but is also essential to understand the energy source for the excitation of whistler-mode chorus waves, one of the most important plasma waves in accelerating radiation belt electrons (e.g., Bortnik & Thorne, 2007; Horne et al., 2005; Reeves et al., 2013; Thorne et al., 2013). Chorus waves, often occurring in two frequency bands (lower-band, ~ 0.1 – $0.5 f_{ce}$, and upper-band, ~ 0.5 – $0.8 f_{ce}$, where f_{ce} is the electron cyclotron frequency), are frequently present outside the plasmasphere (e.g., O. Agapitov et al., 2013; Burtis & Helliwell, 1969; W. Li et al., 2009; Meredith et al., 2012; Tsurutani & Smith, 1977). Electrons of 1–10s of keV energies with sufficient flux and anisotropy are believed to play the most crucial role in generating chorus waves through cyclotron resonance (e.g., Kennel & Petschek, 1966; W. Li et al., 2009; Yue et al., 2016). Statistical global maps of chorus waves have been constructed by several studies using in situ measurements from various satellites (e.g., O. Agapitov et al., 2013; Aryan et al., 2014; W. Li et al., 2009; Meredith et al., 2012, 2003). It has also been shown that event-specific global maps of chorus waves can also be proxied by the observed ~ 10 s of keV electron precipitation distribution (e.g., Chen, Friedel, et al., 2014; Chen, Reeves, et al., 2014; W. Li et al., 2013). These studies clearly showed the enhancement of chorus wave intensity during geomagnetic active times, most commonly around the dawn sector, which is consistent with the enhanced electron drift and suggesting the vital role of electron cyclotron resonance in generating chorus waves.

In this study, using data from the Helium, Oxygen, Proton, and Electron (HOPE) mass spectrometer (Funsten et al., 2013; Spence et al., 2013) on the Van Allen Probe—A, we examined the equatorial PADs of ~ 1 – 50 keV electrons in Earth's inner magnetosphere through statistical analysis. Measured electron PADs have been propagated to the magnetic equator and then averaged in 5 min, assuming symmetric PADs around 90° pitch angles. A Legendre polynomial form has been adopted to fit each equatorial PAD, and

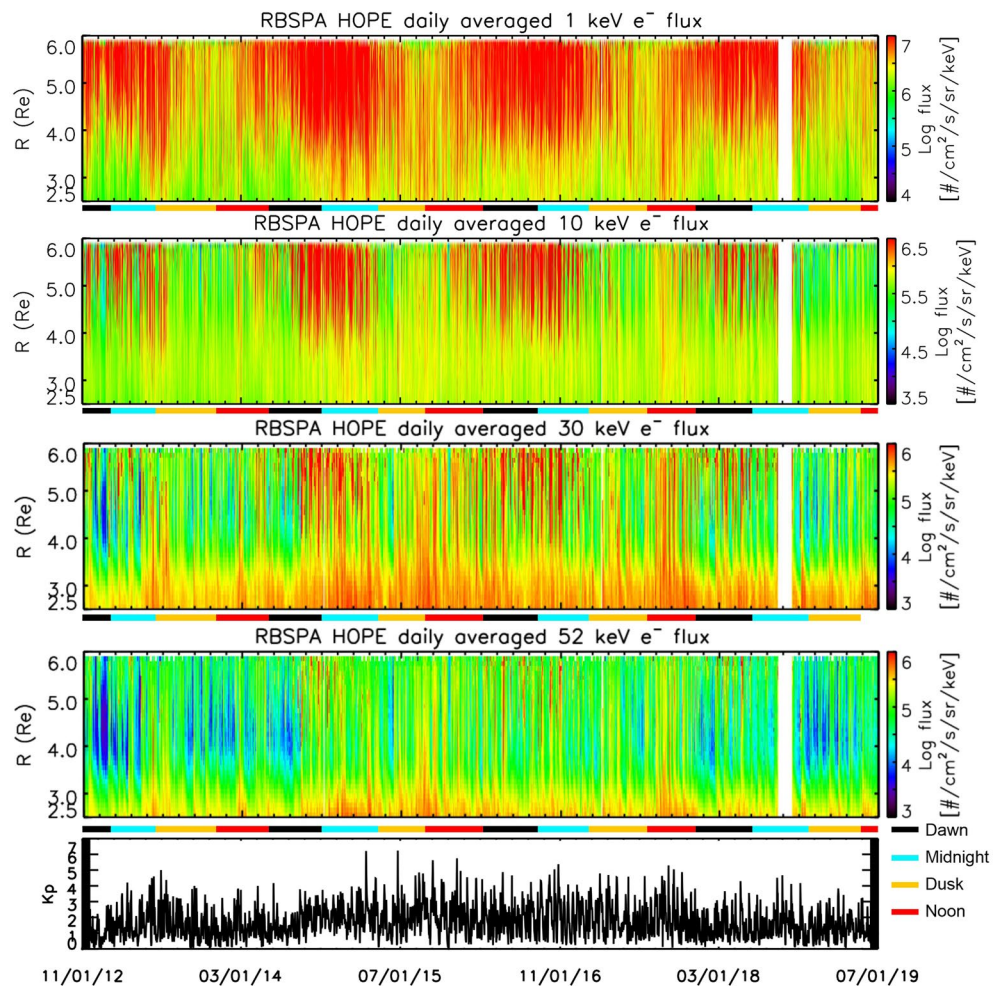


Figure 2. Daily averaged fluxes of ~ 1 , 10, 30, and 52 keV electrons using HOPE measurements on the Van Allen Probe—A from November 1, 2012 to July 1, 2019, along with the daily averaged Kp index. The colored lines underneath each panel show the MLT sector of Van Allen Probe—A's apogee: dawn (black), midnight (blue), dusk (yellow), and noon (red). HOPE, Helium, Oxygen, Proton, and Electron.

the resulted coefficients of Legendre polynomials are binned in the radial distance (R), magnetic local time (MLT), geomagnetic activity indicated by the Kp index, and electron energy (E). The medians, means, and standard deviations of coefficients in each (R , MLT, Kp, and E) bin are derived, with which the empirical electron PADs can be reconstructed. Based on model results, the characteristics of ~ 1 – 10 s of keV electron equatorial PADs in the inner magnetosphere are presented, and the role of these electrons in chorus wave excitation is discussed. Data and methodology used to construct this empirical electron PAD model are shown in Section 2. Model results and implications are discussed in Section 3. Section 4 is the summary.

2. Data and Methodology

Pitch-angle-resolved electron fluxes (level 3, rel04 version) from the HOPE mass spectrometer on the Van Allen Probe—A from November 2012 to June 2019 were used in this study. The Van Allen Probes operated in a geotransfer-like orbit with an inclination of $\sim 10^\circ$, a perigee of ~ 600 km, and an apogee of $\sim 5.8 R_E$ (Mauk et al., 2012). The spacecraft's spin period was ~ 11 – 12 s, with the spin axis approximately pointing to the Sun. HOPE mass spectrometer provided in situ flux measurements of electrons and ions with energies of ~ 1 eV–50 keV. Figure 2 shows the daily averaged fluxes of electrons with different energies as a function of radial distance R and time using HOPE—A measurements during this period. The MLT sector where Van

Allen Probe—A's apogee was located is indicated by the colored line underneath each panel. The bottom panel of Figure 2 shows the daily averaged Kp index, using data from OmniWeb. Figure 2 clearly shows that these 1–10s of keV energetic electrons are very dynamic in Earth's inner magnetosphere, and they also clearly exhibit energy-dependent acceleration, loss, and transport processes. During geomagnetically active times, the enhancements of electron fluxes are more dominant, and these energetic electrons also tend to penetrate deeper into the inner magnetosphere. Specifically, the electron fluxes at larger radial distances were higher when the apogee of Van Allen Probe—A was located near midnight to dawn. This is consistent with the drift pattern of 1–10s of keV electrons: under the influence of large-scale convection electric field, these energetic electrons drift eastward toward dayside through dawn after being injected from the night-side plasmashet, and they also penetrate deeper into the inner magnetosphere during geomagnetically active times (e.g., Korth et al., 1999).

To study the statistical properties of electron equatorial PADs, a method of Legendre polynomial fitting has been applied to represent each PAD as a set of Legendre polynomials, then the coefficients of Legendre polynomials have been recorded and statistically analyzed. Various methods have been used in previous studies to categorize PADs (e.g., Gannon et al., 2007; Sarno-Smith, Larsen, et al., 2016; Sarno-Smith, Liemohn, et al., 2016; Zhao et al., 2014b, 2014a). However, several properties of Legendre polynomials make them ideal for representing electron PADs. First, any function can be represented by a completed set of Legendre polynomials, and previous studies have well demonstrated that a set of Legendre polynomials up to sixth order are sufficient to represent electron PADs in the outer belt (Chen, Friedel, et al., 2014; Chen, Reeves, et al., 2014; Zhao et al., 2018). Second, Legendre polynomials have definite parity: the symmetry of even-order Legendre polynomials makes them ideal to fit PADs that are often symmetric around 90° PA. Third, the coefficients of Legendre polynomials are very useful in identifying the PAD shapes and assessing the anisotropy of particles, which will be further discussed below.

The PAD can be expressed using Legendre polynomials as (Chen, Friedel, et al., 2014; Chen, Reeves, et al., 2014; Zhao et al., 2018):

$$j(\alpha) = \sum_{n=0}^{\infty} C_n P_n[\cos(\alpha)]$$

where α is PA, $j(\alpha)$ is the differential flux of particles with PA α , $P_n[\cos(\alpha)]$ is the n th-order Legendre polynomial, and C_n is the coefficient of n th-order Legendre polynomial which can be calculated using

$$C_n = \frac{2n+1}{2} \int_0^{\pi} j(\alpha) P_n[\cos \alpha] \sin \alpha d\alpha$$

Since we focus on the electron PAD shapes in this study, we further normalize the coefficients of Legendre polynomials as

$$c_n = C_n / C_0$$

where C_0 is the directionally averaged flux. Once the normalized coefficients of Legendre polynomials have been derived, a normalized PAD, $j'(\alpha)$, can be reconstructed as:

$$j'(\alpha) = \sum_{n=0}^{\infty} c_n P_n[\cos(\alpha)]$$

In this study, assuming electron PADs are symmetric, we use a combination of Legendre polynomials P_2 , P_4 , and P_6 to fit electron PADs and construct a statistical model of coefficients c_2 , c_4 , and c_6 . This assumption is mostly valid: for 1–10s of keV electron PADs, >90% of fits using Legendre polynomials P_2 , P_4 , and P_6 have a truncated error <10% compared to the observations.

Figure 1 also shows examples of Legendre polynomial fitting results of three main types of PADs. The fitting results are shown in red curves, and the corresponding normalized coefficients c_1 – c_6 are shown at the top of each panel. Note that the observations of PADs (black crosses) have been averaged in 5 min, assuming that they are symmetric around 90° PA. These fitting results show great agreement to the observations,

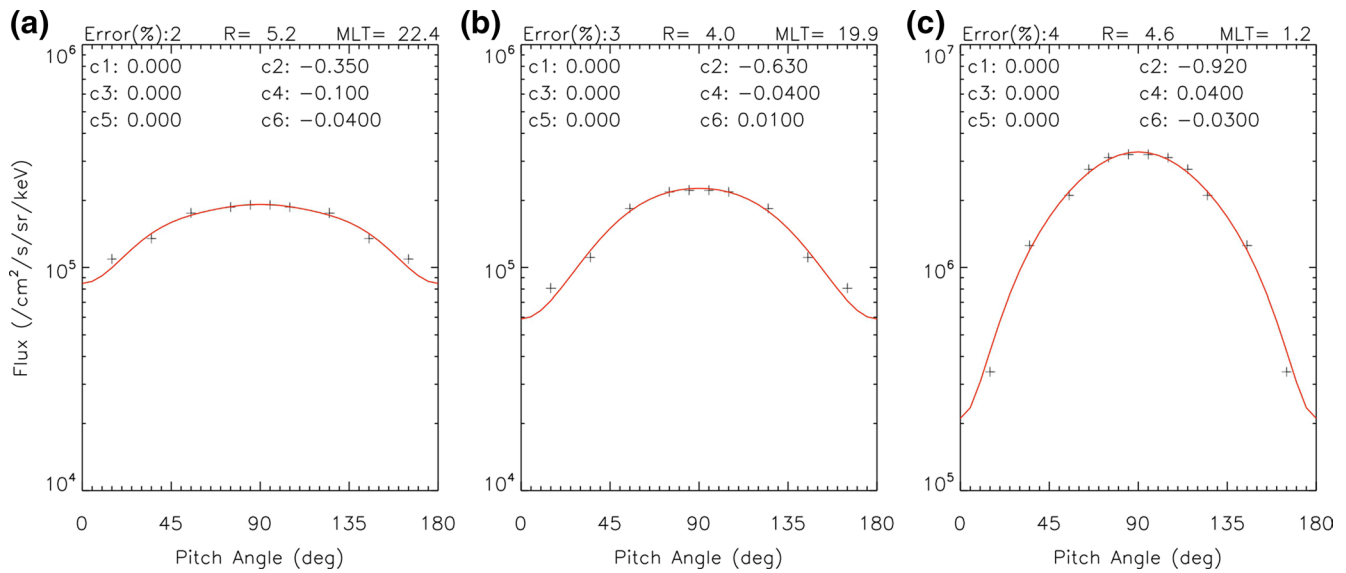


Figure 3. Examples of electron PADs of various anisotropy and the corresponding Legendre polynomial fitting results. The format is similar to Figure 1. PAD, pitch angle distribution.

validating the Legendre polynomial fitting method. The coefficients c_1 , c_3 , and c_5 are all zeros, also validating the Legendre polynomial fitting results. Figure 1 also demonstrates that the coefficients of Legendre polynomials can be used to identify the PAD type: the pancake PAD has negative c_2 and near-zero c_4 (Figure 1a); the flattop PAD has negative c_2 and c_4 (Figure 1b); the butterfly PAD has near-zero c_2 and negative c_4 (Figure 1c).

Besides, the coefficient c_2 of Legendre polynomial fitting results can also be used to assess the anisotropy of the electron distribution. Figure 3 shows examples of electron PADs with various c_2 . From Figures 3a–3c, c_2 becomes more negative (or the absolute value of c_2 gets higher), and the PAD becomes more excessively peaked at 90° PA, suggesting a more anisotropic electron distribution.

Using electron flux data from the HOPE instrument on the Van Allen Probe—A, the equatorial PADs of electrons with energies of ~ 1 –50 keV have been studied statistically. As we mainly focus on > 1 keV electrons, the impact of spacecraft charging on the electron flux measurements can be ignored (e.g., Sarno-Smith, Larsen, et al., 2016; Sarno-Smith, Liemohn, et al., 2016). The measured electron PADs are first propagated to geomagnetic equator using the T89D model (Tsyganenko, 1989) with the relation

$$\frac{\sin^2 \alpha_{\text{local}}}{B_{\text{local}}} = \frac{\sin^2 \alpha_{\text{eq}}}{B_{\text{eq}}}$$

where α_{local} and α_{eq} are local and equatorial pitch angles, and B_{local} and B_{eq} are local and equatorial magnetic field magnitudes. Then, these equatorial PADs are averaged in 5 min to ensure enough statistics, assuming symmetric PADs around 90° PA. Using the method of Legendre polynomial fitting, each 5-min-averaged equatorial PAD is represented by a set of coefficients c_2 , c_4 , and c_6 . Then, an empirical model of these coefficients has been constructed statistically. Several measures have been applied to ensure both the PAD and the fit are valid: we have only included PADs (1) with enough counts (averaged counts of a PAD > 50); (2) measured close to the geomagnetic equator ($-10^\circ < \text{magnetic latitude} < 10^\circ$); (3) with a wide PA range (have measurements at both large PAs [80° – 100°] and small PAs [0° – $20^\circ/160^\circ$ – 180°]); (4) are well fit by Legendre polynomials up to sixth order with a root-mean-square-deviation (RMSD) < 0.1 , where

$$\text{RMSD} = \sqrt{\frac{\sum_m (\log \hat{j} - \log j)^2}{m}}$$

Table 1
The Values of the Electron Equatorial PAD Model Parameters

Parameter	Value
Radial distance R (R_E)	2.6, 2.8, 3.0, ..., 5.8 (± 0.1)
Magnetic local time MLT	0, 2, 4, ..., 22 (± 1)
Geomagnetic activity Kp	Kp $\leq 1+$, $1+ < Kp \leq 3+$, and Kp $> 3+$
Electron energy E (keV)	1, 3, 5, 10, 15, 20, 30, 40, and 52

Abbreviation: PAD, pitch angle distribution.

j is the observed flux, \hat{j} is the fitted flux, and m is the number of data points used in the fitting.

Using HOPE—A data from November 2012 to June 2019, a statistical equatorial PAD model of ~ 1 –50 keV electrons has been constructed as a function of radial distance R, magnetic local time MLT, geomagnetic activity represented by Kp, and electron energy E. Here we choose to use the radial distance R instead of the commonly used L-shell, since for 1–10s of keV electrons the influence from large-scale DC electric fields on their drift paths cannot be ignored, thus, the use of L-shell calculated based on the geomagnetic field alone may not be appropriate for these low-energy electrons. The values of model parameters are shown in Table 1. Here we focus on results at $R > 2.5 R_E$ only, as the potential contamination of

HOPE electron measurements at lower altitudes may hinder the identification of PADs (Boyd et al., 2019). The medians, means, and standard deviations of fitting coefficients have been derived for each (R, MLT, Kp, and E) bin with the number of valid PADs greater than 10. The model results can be found at <https://zenodo.org/record/3884260>, along with sample programs to demonstrate the usage of the model. In the following section, we will show some model results and further discuss the implications.

3. Model Results

Figure 4 shows the model results of the medians of coefficients c_2 , c_4 , and c_6 in each R, MLT, Kp bin for 1 keV electrons, during geomagnetically quiet (Kp $\leq 1+$), moderate ($1+ < Kp \leq 3+$), and active times (Kp $> 3+$). The ratios of good fits (RMSD < 0.1) to all fits are shown in the top left corner of each panel in the first row. These high ratios suggest overall good fits of electron PADs, further validating the Legendre polynomial fitting method. Note that, under geomagnetically active conditions, this ratio occasionally drops close to 50% at some L-MLT bins. This is likely caused by the highly dynamic nature of these keV–10s of keV electrons during active times, suggesting the complexity of inner magnetospheric dynamics. It may also be related to some transient features of energetic electrons in the inner magnetosphere, for example, injections. The number of PADs used in each bin in constructing this empirical model is displayed in the top right corner, showing overall good statistics. Standard deviations of corresponding coefficients are shown in the bottom right corner of each panel, which can be used to assess the variabilities of PADs.

Several intriguing features are revealed in Figure 4. First, for 1 keV electrons (and also for up to 10s of keV electrons as shown in Figures 6 and 8), the model results suggest that the majority of PAD fits have a significantly negative c_2 with a c_4 of a much smaller magnitude: the median of c_2 in each (R, MLT, and Kp) bin is mostly smaller than -0.5 , while the median of c_4 is commonly near zero. This indicates that the majority of ~ 1 –10s of keV electron equatorial PADs are pancake PADs in the inner magnetosphere. It is very different from the results of relativistic electrons: Zhao et al. (2018), using observations from the Van Allen Probes and the same fitting method, showed that for MeV electron equatorial PADs the coefficient c_2 is often near zero or even positive at night side at higher L; combining with a mostly negative c_4 , this indicates that MeV electrons commonly exhibit butterfly PADs at night side at larger L. Such differences between MeV electrons and 1–10s of keV electrons could be caused by the different radial gradient in electron fluxes: as shown in Figure 2, 1–10s of keV electrons often have relatively flat or positive radial flux gradients at higher L; such radial flux gradients, even combined with the drift shell splitting effect, will not produce significant butterfly PADs. On the other hand, comparing to MeV electrons, 1–10s of keV electrons are subject to more substantial influence from the large-scale DC electric fields. Thus, the differences in PADs could also result from the convection electric field and the associated electron drift (e.g., Califf et al., 2017, 2014; Korth et al., 1999; Zhao et al., 2017).

On the other hand, previous studies have suggested the existence of cigar PADs of 10–100s of keV electrons at high L-shells, with flux peaking along the local magnetic field direction (e.g., Baker et al., 1978, 1981). These studies showed that these cigar PADs were observed near substorm onset and may be caused by the tail-like stretching of the nightside magnetic field. Our results, however, do not show prevalent cigar PADs

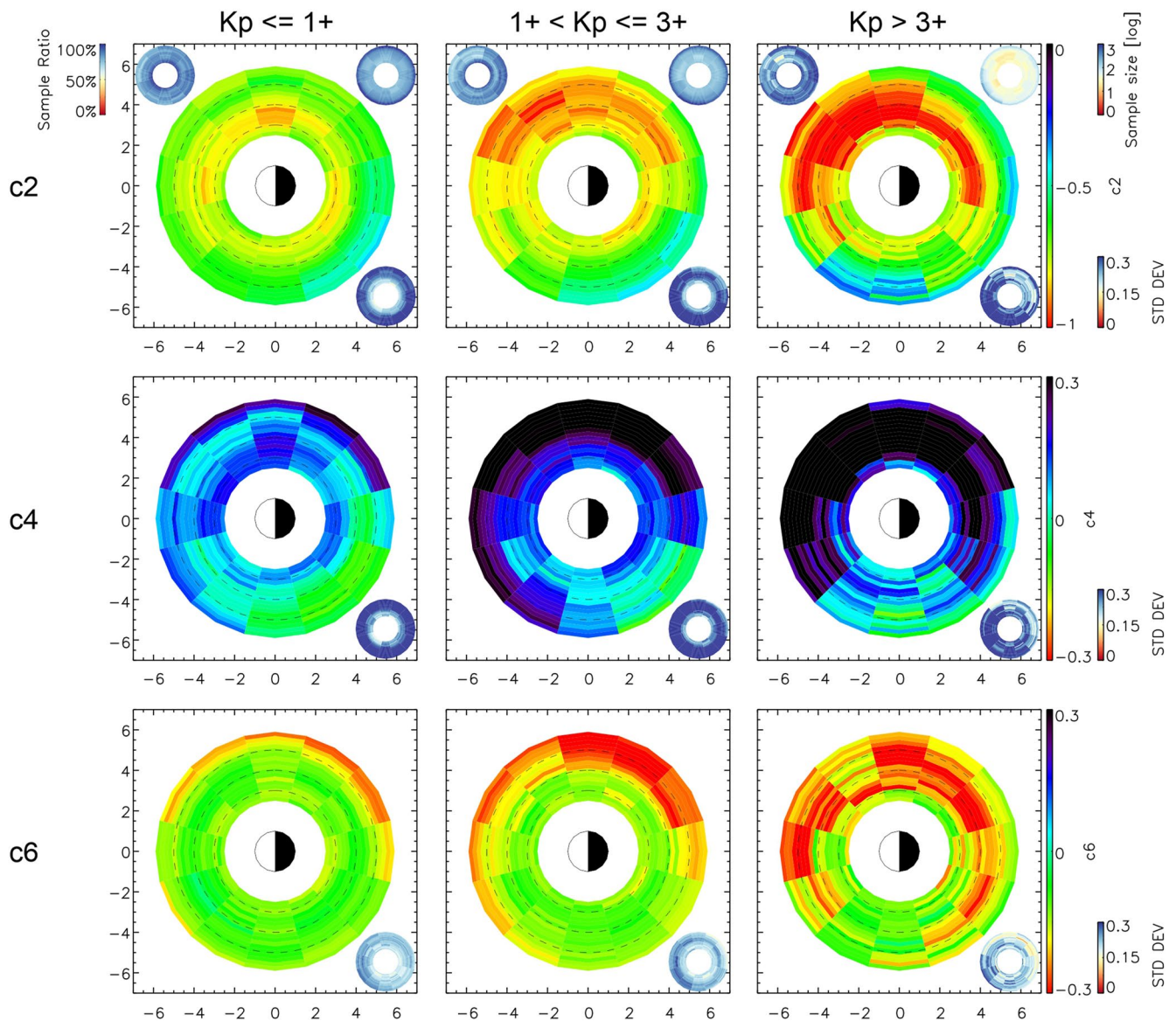


Figure 4. The medians of coefficients c_2 , c_4 , and c_6 of 1 keV electron PAD model. Three columns correspond to three geomagnetic activity levels: $K_p \leq 1+$, $1+ < K_p \leq 3+$, and $K_p > 3+$. The small ring in the top left corner of each panel of c_2 shows the ratio of good fits (RMSD < 0.1) to all fits. The ring in the top right corner shows the number of PADs included in each bin. The ring in the bottom right corner of each panel shows the standard deviation of the corresponding coefficient in each bin. Dashed circles in each panel show $R = 3, 4,$ and $5 R_E$ PAD, pitch angle distribution.

for 1–10s of keV electrons: less than $\sim 1\%$ of equatorial PADs of 1–10s of keV electrons show features of cigar distribution (with $c_2 > 0.1$). This difference between our study and previous studies may be due to the different location of observations: this study, limited by the Van Allen Probes data, focuses on the region with $R < 5.8 R_E$; while the observations from Baker et al. (1978, 1981) were at geosynchronous orbit. Closer to the Earth, the geomagnetic field is more dipole-like and less stretched during active times. Though the number of observed cigar PADs of 1–10s of keV electrons in this study is small, these PADs were indeed observed mostly at high L at substorm times.

Figure 4 also shows that, for 1 keV electron PADs (and also for 10s of keV electron PADs as shown in Figures 6 and 8), the magnitude of c_2 is often much larger than that of c_4 and c_6 (note that the color bar of c_2 and that of c_4 and c_6 are very different). This further suggests that the anisotropy of 1–10s of keV electrons can be mainly assessed using the coefficient c_2 of fitting results. As the magnitude of c_2 gets larger, the PAD gets

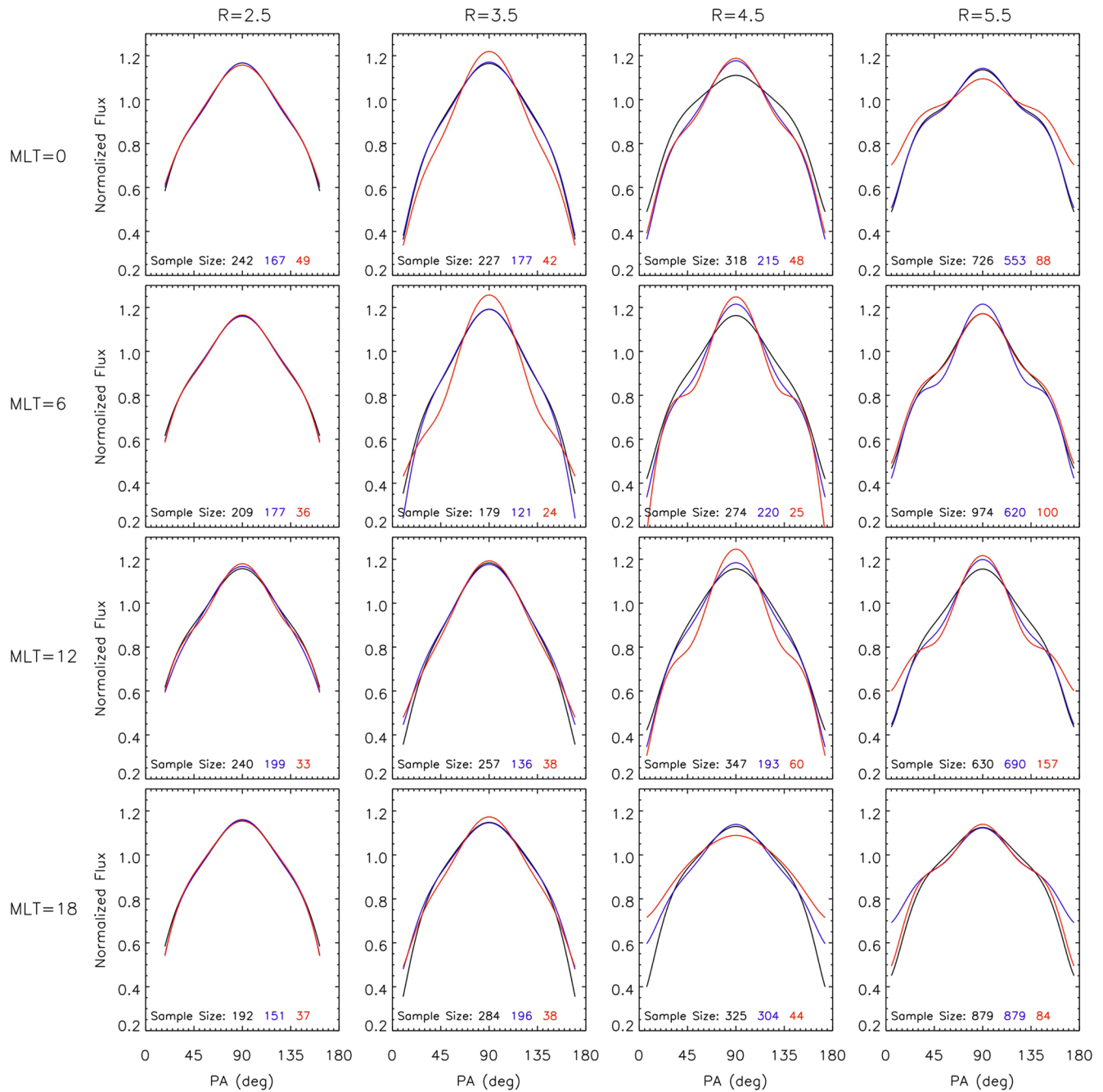


Figure 5. The averaged PADs of 1 keV electrons reconstructed using the medians of coefficients of the electron PAD model. Black curves show the results during quiet times with $K_p \leq 1+$, blue curves show those under moderate activities with $1+ < K_p \leq 3+$, and red curves show the results during active times with $K_p > 3+$. The number of PADs in each condition is listed at the bottom of each panel. Four columns correspond to results at $R = 2.5, 3.5, 4.5,$ and $5.5 R_E$, and four rows show the results at $MLT = 0, 6, 12,$ and 18 . PAD, pitch angle distribution.

more excessively peaked around 90° PA and thus more anisotropic. Thus, in this study, we will be mainly focusing on coefficient c_2 when analyzing model results.

During geomagnetically quiet times, as the first column of Figure 4 shows, 1 keV electron PADs are more anisotropic at lower R, potentially due to larger loss cones at lower altitudes. As the geomagnetic activity gets more intense, 1 keV electron PADs start to get more anisotropic from midnight to dawn and to noon at a wide R range. Under intense geomagnetic activity with $K_p > 3+$, model results show that large anisotropy

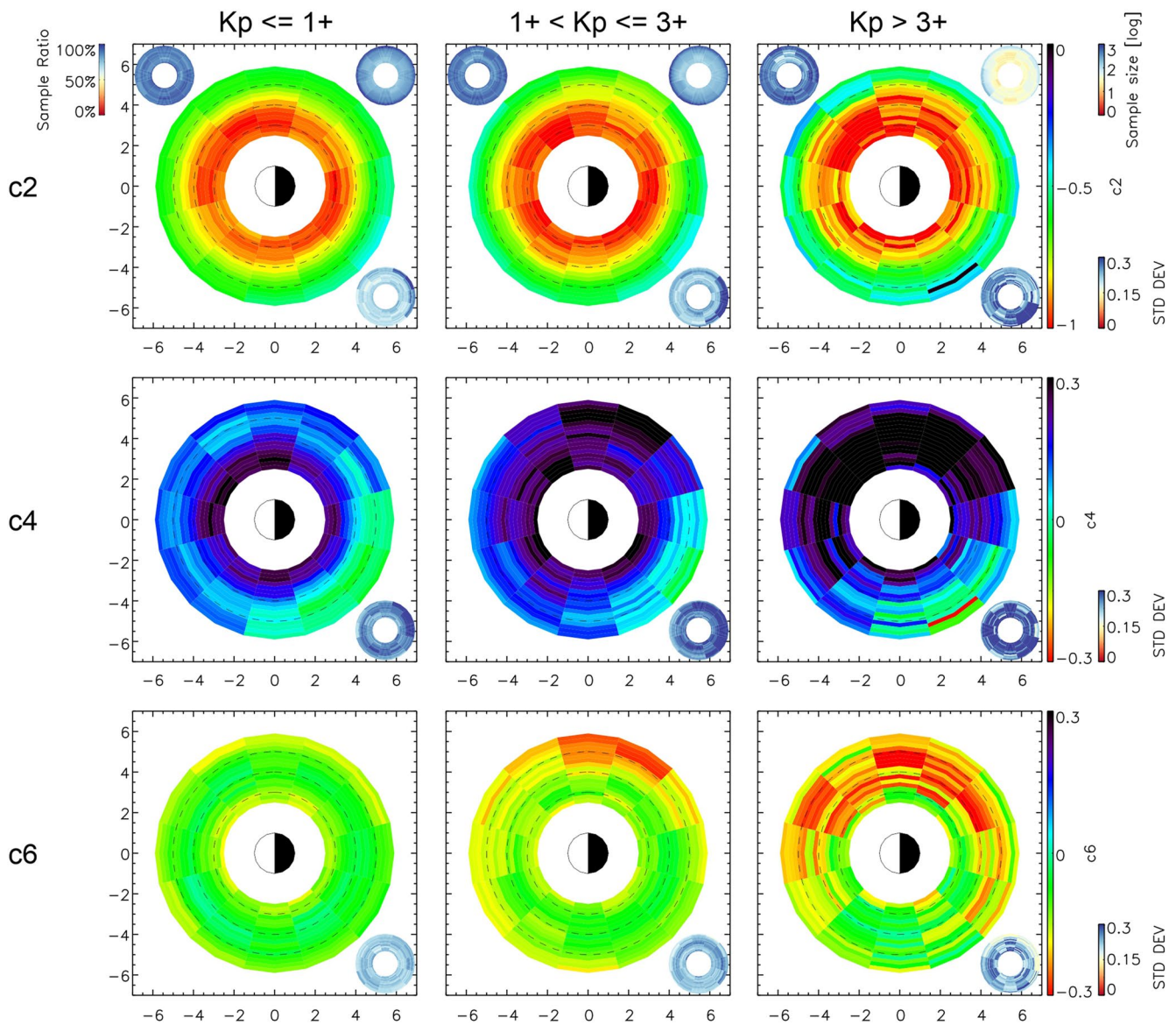


Figure 6. Similar format to Figure 4 but for 5 keV electrons.

exists for 1 keV electrons, and the distribution of such high anisotropy region is R- and MLT-dependent. At $R \sim 3-4 R_E$, more anisotropic PADs exist at a wide MLT range from around midnight to dawn to pre-noon. As R gets higher, the region of large anisotropy in electron PADs starts to shift toward dayside. At $R \sim 4-5.5 R_E$, the PADs are highly anisotropic from dawn to noon. These anisotropic PADs may be a result of particle injection and/or convection under the effect of the enhanced large-scale DC electric field during geomagnetically active times. They can be a potential energy source for the excitation of the plasma waves during active times.

Figure 5 shows the averaged equatorial PADs of 1 keV electrons reconstructed using the medians of coefficients of the model results at various R and MLT. Three different colors indicate three activity levels: $Kp \leq 1+$ (black), $1+ < Kp \leq 3+$ (blue), and $Kp > 3+$ (red). At $R = 2.5 R_E$, 1 keV electron PADs have little variation over different MLT and different activity levels. This suggests that, in the Van Allen Probes era, the geomagnetic activity was not intense enough to strongly influence the dynamics of 1 keV electrons at such low altitudes. At higher R, the results start to show differences under different geomagnetic activity conditions. At $R = 3.5 R_E$, the electron PADs become more excessively peaked around 90° PA at MLT = 0 and 6

during active times. At $R = 4.5 R_E$, more anisotropic PADs exist at MLT = 0, 6, and 12 during active times; while intriguingly, the PAD at MLT = 18 becomes less anisotropic during active times than that during quiet times. At $R = 5.5 R_E$, enhanced geomagnetic activity has a mixed effect on electron PADs, causing larger anisotropy mainly around MLT = 12. These results are consistent with Figure 4 and suggest the effects of enhanced convection or injection during active times. Also, note that the head-and-shoulder (or cap) PADs can be observed at some R and MLT bins mostly during active times. These head-and-shoulder PADs could be caused by plasmaspheric hiss wave scattering inside the plasmasphere (e.g., Lyons & Williams, 1975; Zhao et al., 2014b) or a combination of the drift-shell-splitting effect and a substorm injection or a sudden magnetospheric compression (Sibeck et al., 1987).

Figure 6 shows the model results of 5 keV electron PADs in a similar format to Figure 4. During quiet times, the PADs with large anisotropy are often located at $R < 4 R_E$, and slight day-night asymmetry in PADs can be observed. Comparing to 1 keV electron PADs, 5 keV electron PADs are more anisotropic at the lower R region. As the geomagnetic activity gets more intense, the anisotropy of electron PADs at larger R at midnight to dawn gets more significant, while near dusk, the electron PADs flatten. Again, this may be related to the enhanced convection electric field and associated variations of electron drift paths during active times. It may also be caused by injections of 5 keV electrons into the inner magnetosphere during active times, which preferentially occur near midnight to dawn. Note that the patterns of regions with enhanced anisotropy during active times are very different for 1 and 5 keV electrons: at $R \sim 4\text{--}5.8 R_E$, the anisotropy of 1 keV electron PADs enhances the most at dawn to noon, while 5 keV electron PADs get more excessively peaked around midnight to dawn at a narrower R range ($R \sim 4\text{--}5 R_E$); at lower R , however, 5 keV electron PADs change little under different geomagnetic activities, while 1 keV electrons still get more anisotropic at $R \sim 3\text{--}4 R_E$ at a relatively wide MLT range (\sim midnight to prenoon). These differences may be related to the different drift patterns of electrons with different energies: electrons with lower energies are subject to more significant influence from the electric field and often drift closer to Earth when the convection electric field enhances (e.g., Korth et al., 1999; Zhao et al., 2017). They may also be caused by deeper, more frequent injections of lower-energy electrons during active times (e.g., Reeves et al., 2016; Turner et al., 2015; Zhao et al., 2016).

Figure 7 shows the averaged PADs of 5 keV electrons reconstructed using the model results in a similar format to Figure 5. At $R = 2.5 R_E$, little variation in PADs can be observed; thus, we only show results at $R = 3.5, 4.5,$ and $5.5 R_E$. At $R = 3.5 R_E$, for 5 keV electrons, the averaged PAD does not change much under different geomagnetic activities. At $R = 4.5 R_E$, during active times, more excessively peaked PADs can be observed at dawn and midnight; while at dusk, PAD gets less anisotropic. At $R = 5.5 R_E$, the variations in electron PADs are not very significant, while it is still intriguing to see more flattened PADs at noon and dusk.

The medians of coefficients of 30 keV electron PADs are shown in Figure 8. At geomagnetically quiet times, similar to 5 keV electrons, 30 keV electron PADs are also more anisotropic at lower R region ($R < 4 R_E$), and day-night asymmetry can be clearly observed at larger R . As the geomagnetic activity gets more intense, the electron PADs become more excessively peaked around 90° PA at $R > 4 R_E$ from midnight to dawn; while around dusk, the PADs get more flattened. The averaged PADs shown in Figure 9 also clearly demonstrate these features. At $R = 3.5 R_E$, little variation can be seen under different geomagnetic activity, while at MLT = 6, the PAD gets slightly more anisotropic during active times. At $R = 4.5 R_E$, significant differences exist in PADs under different geomagnetic activity levels: at midnight and dawn, the electron distribution gets more anisotropic during active times; at dusk, the electron PAD flattens as geomagnetic activity enhances. At $R = 5.5 R_E$, enhanced anisotropy in electron PADs can still be observed at midnight and dawn during active times.

The anisotropy of 1–10s of keV electrons plays a critical role in chorus wave excitation in the inner magnetosphere. It is commonly believed that the chorus wave in the inner magnetosphere is mainly generated by the cyclotron resonance of 1–10s of keV electrons with sufficient flux and anisotropy. Many studies have examined the statistical distribution of chorus wave intensities under various geomagnetic conditions (e.g., O. V. Agapitov et al., 2015; Aryan et al., 2014; W. Li et al., 2009; Meredith et al., 2012, 2003; Wang et al., 2019). Meredith et al. (2012), using data from multiple satellites including the Dynamics Explorer 1, the Combined Release and Radiation Effects Satellite (CRRES), Cluster, Double Star, and the Time His-

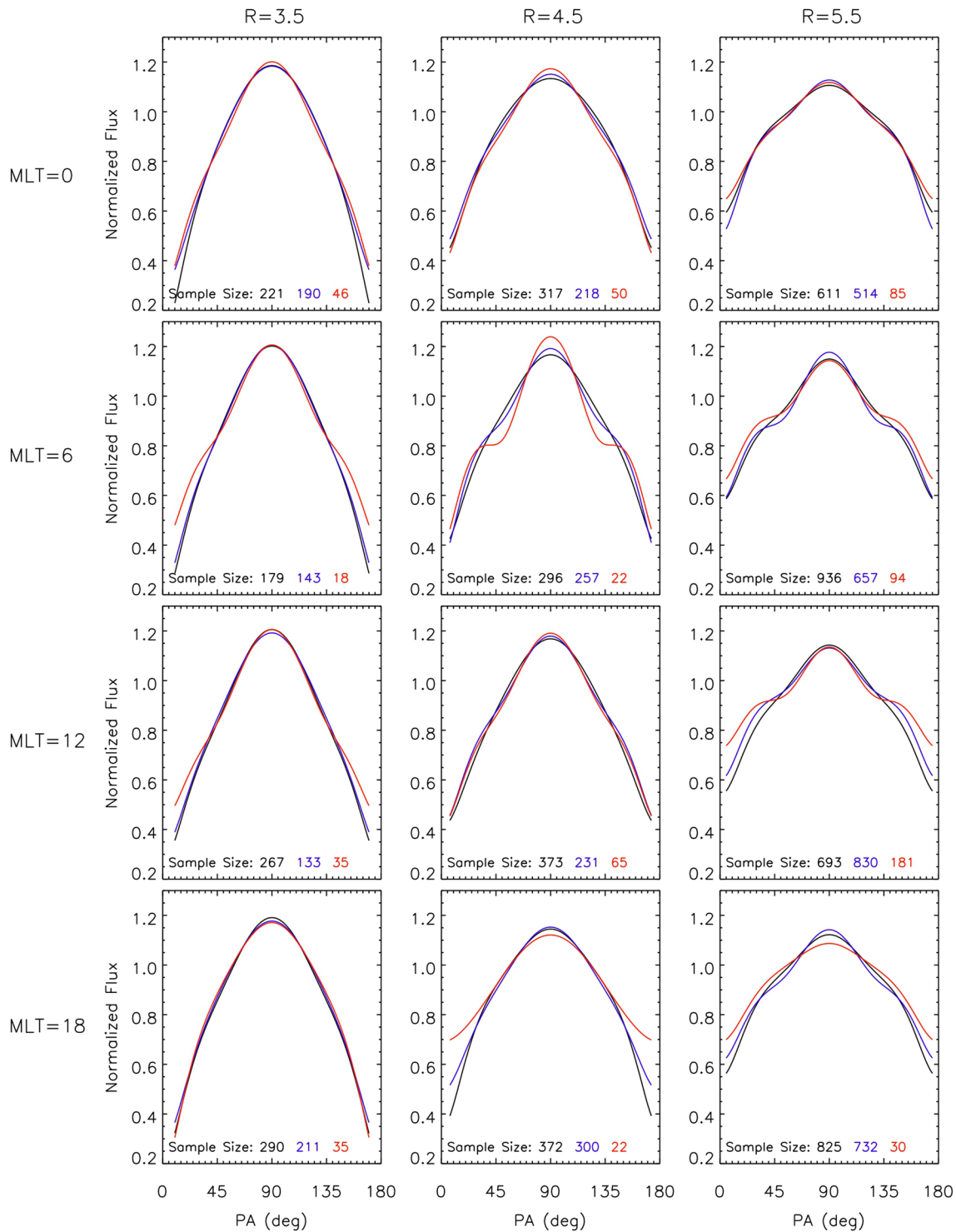


Figure 7. Similar format to Figure 5 but for 5 keV electrons.

tory of Events and Macroscale Interactions during Substorms (THEMIS), showed that the chorus waves are often much stronger during geomagnetically active times. Statistically, during active times with $AE > 300$ nT, the near-equatorial (magnetic latitude $\sim -15^\circ$ – 15°) lower-band chorus wave intensity peaks at 2300 to 1200 MLT at $L \sim 4$ – 9 , and the equatorial upper-band chorus wave intensity peaks at similar MLT region

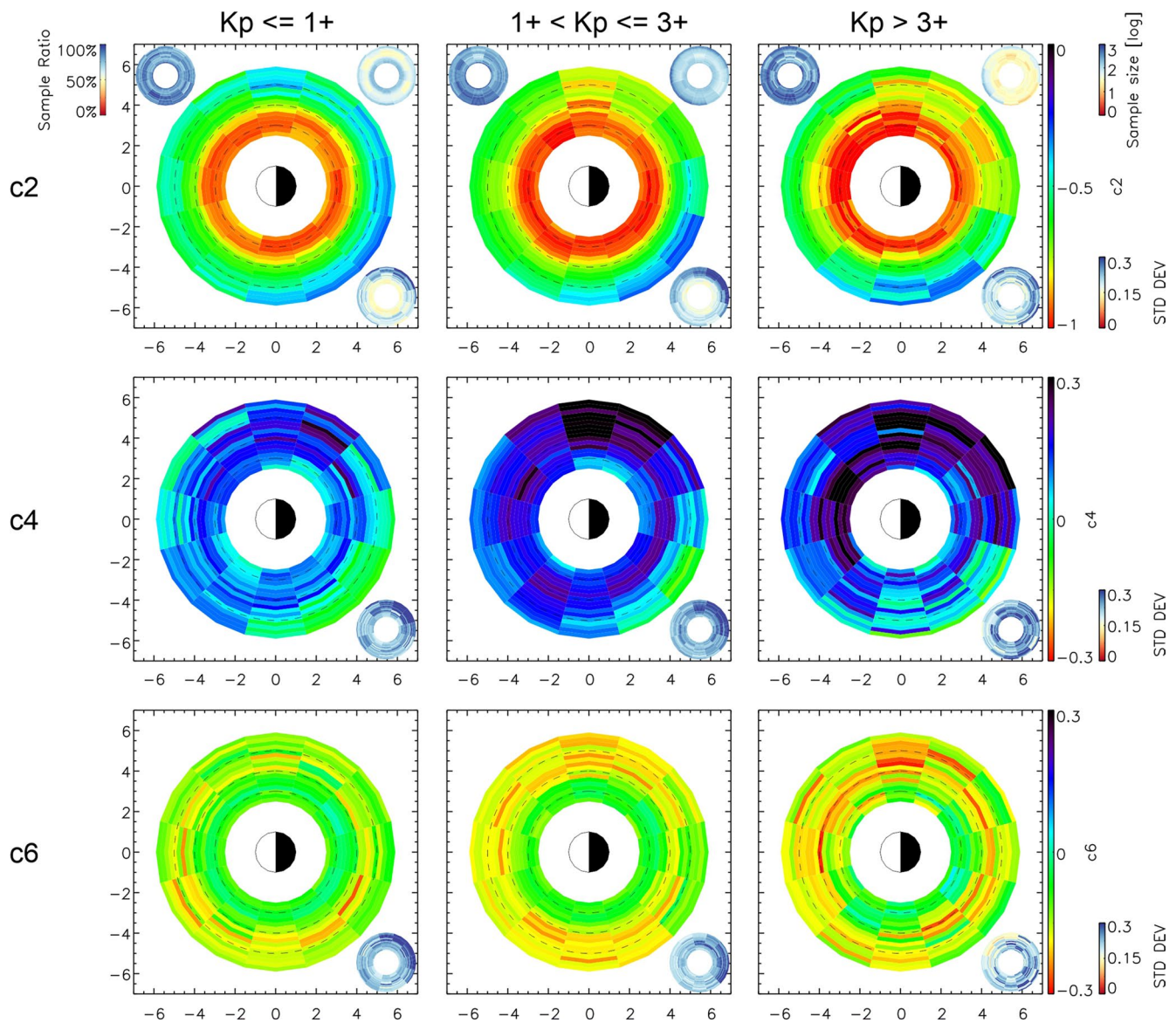


Figure 8. Similar format to Figure 4 but for 30 keV electrons.

at $L \sim 3-7$. While the midlatitude (magnetic latitude $\sim 15^\circ-30^\circ$) chorus waves are mainly in the lower band with peak intensity at 0700–1400 MLT at $L \sim 4-9$. Their results are consistent with our observations of the statistical distribution of 1–10s of keV electron PADs. The anisotropy of 1–10s of keV electrons strongly enhances during geomagnetically active times, which can be responsible for generating more intense chorus waves through electron cyclotron resonance. Different MLT patterns of high anisotropy region are also observed for electrons of different energies. The anisotropy of 5 and 30 keV electrons gets larger at midnight to dawn during active times at $R > \sim 4 R_E$, consistent with the statistical distribution of intense near-equatorial chorus waves shown in Meredith et al. (2012). While for 1 keV electrons, their anisotropy enhances mainly from dawn to noon at $R > 4 R_E$ during active times, similar to the distribution of mid-latitude chorus waves. These results suggest the differential roles of electrons with different energies in generating near-equatorial and midlatitude chorus waves. On the other hand, chorus waves mainly propagate approximately parallel to the local geomagnetic field; however, highly oblique chorus waves have also been observed at mid to high latitudes during disturbed times at $L \sim 4-5.5$ (e.g., Hayakawa et al., 1984; Santolik et al., 2009; O. Agapitov et al., 2013, 2015). J. Li et al. (2016) and W. Li et al. (2016), combining observations from the Van Allen

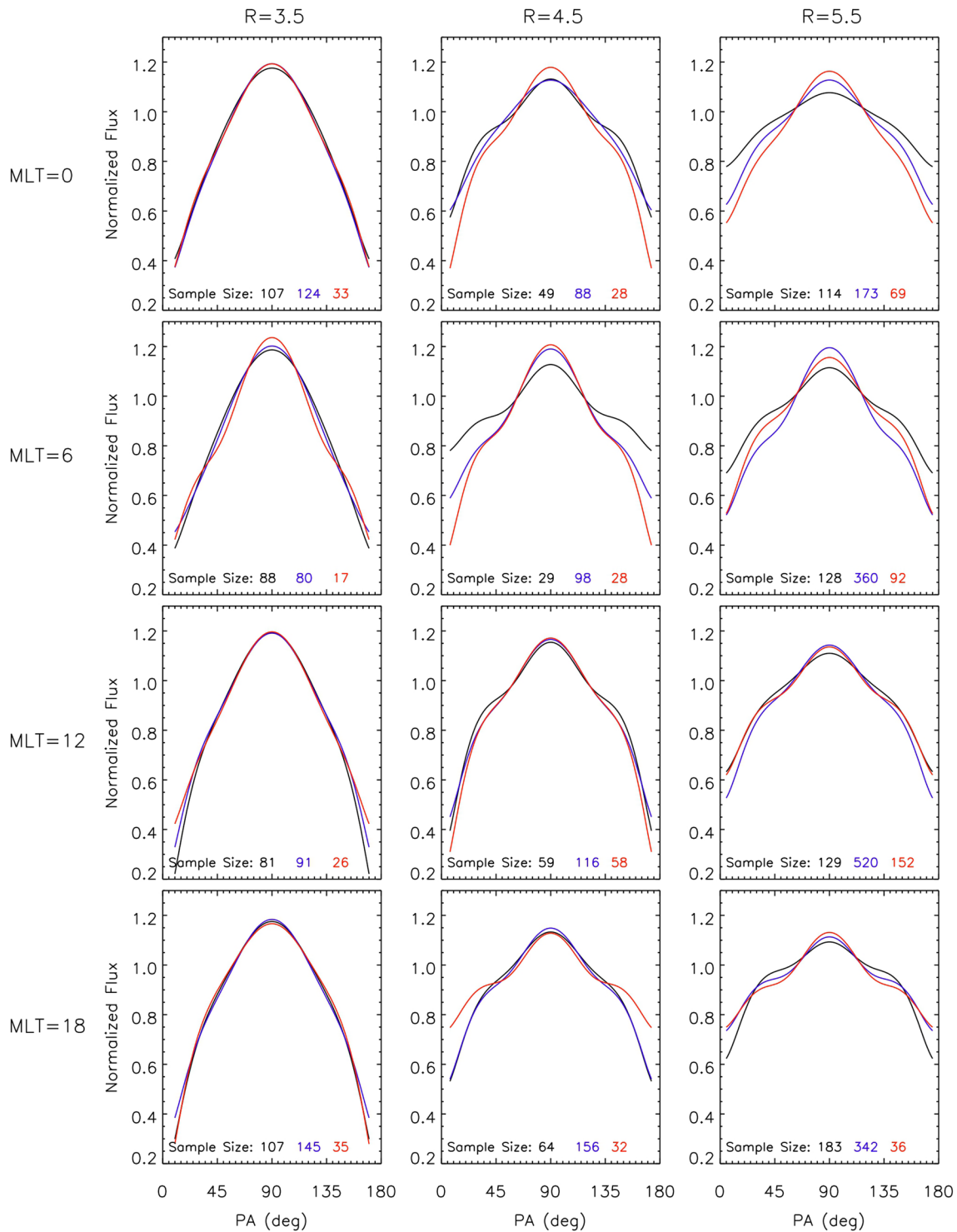


Figure 9. Similar format to Figure 5 but for 30 keV electrons.

Probes with simulations, showed that the cyclotron resonance of electrons with a temperature anisotropy at keV energies could be an excitation mechanism for this highly oblique chorus waves. Our results show that such a temperature anisotropy of keV electrons commonly exists at $R \sim 4\text{--}5.8 R_E$ at dawn to noon during geomagnetically disturbed times, consistent with the much stronger highly oblique chorus waves observed at

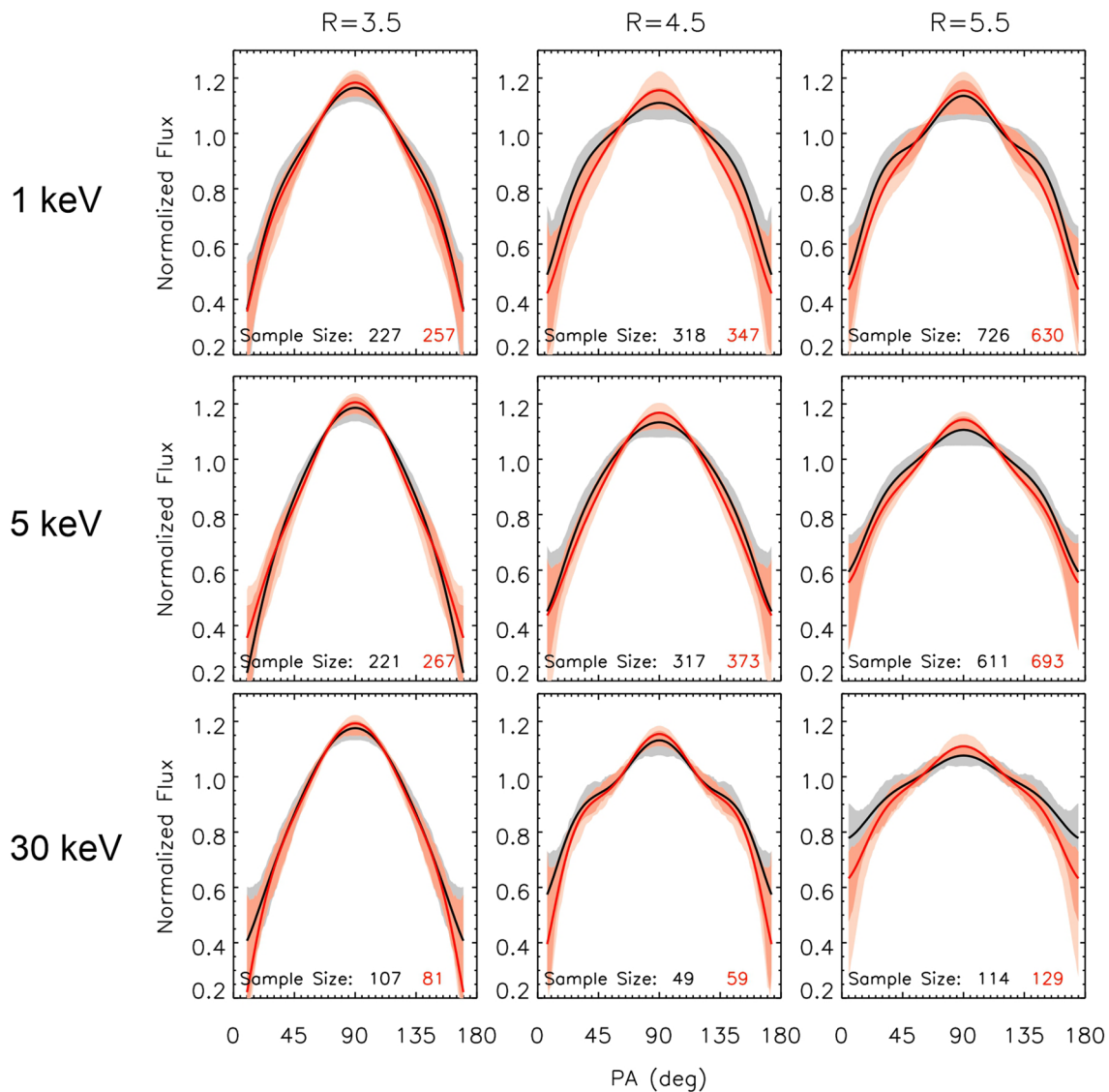


Figure 10. Comparison of electron averaged PADs at noon (red) and midnight (black) under quiet geomagnetic activity. Solid lines are modeled PADs reproduced using medians of coefficients, and shaded areas show the regions between 25th and 75th percentiles. PAD, pitch angle distribution.

0300–1500 MLT than at 1500–0300 MLT by O. V. Agapitov et al., (2015), which further supports that the temperature anisotropy of keV electrons could be responsible for the excitation of highly oblique chorus waves.

Focusing on the day-night comparison of electron PADs, Figures 10 and 11 show the comparisons of averaged PADs at midnight (black curves) and noon (red curves) for electrons of different energies under quiet times ($K_p \leq 1+$) and active times ($K_p > 3+$), respectively. To assess the variability of PADs, the region between 25th and 75th percentiles of PADs in each bin is also shaded in these figures with corresponding colors. Figure 10 shows that, under quiet geomagnetic condition, at $R = 3.5 R_E$, the differences in keV–10s of keV electron PADs at midnight and noon are minimal; however, at larger R , the PADs are relatively steeper at noon than midnight. Such a more significant anisotropy at dayside could be a preferable condition to excite whistler-mode chorus waves. W. Li et al. (2009) studied the statistical distribution of chorus waves and found that moderate chorus waves are often present at dayside even during geomagnetically quiet times. Our observations of higher anisotropy of 1–10s of keV electrons at high R at dayside confirm that the natural enhancement of electron anisotropy could be one of the mechanisms that are responsible for the excitation of these dayside chorus waves.

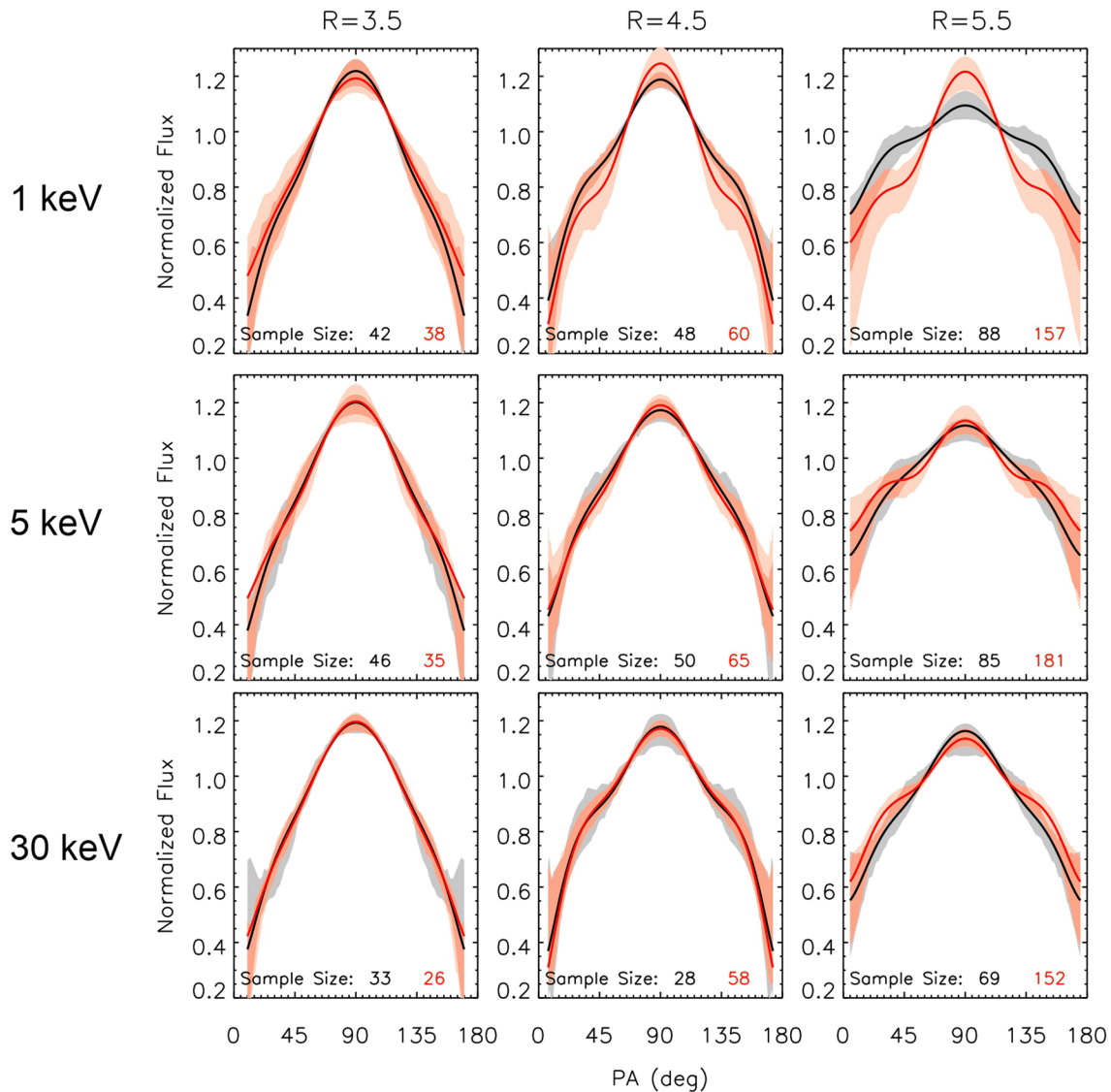


Figure 11. Similar format to Figure 10 but for geomagnetically active times.

During active times, as shown in Figure 11, much stronger anisotropy at dayside can be observed for 1 keV electrons at high R, providing a much more favorable condition for chorus waves to develop. However, for 5 keV and 30 keV electrons, the differences in PADs at midnight and noon diminish, and PADs even flatten slightly at $R = 5.5 R_E$ at dayside. These may be related to different drift patterns of electrons with different energies caused by the enhanced large-scale DC electric fields. These could also be caused by stronger wave-particle interactions during active times.

Figures 12 and 13 show comparisons of averaged PADs and their uncertainties at dusk (black curves) and dawn (red curves) during quiet and active times, respectively. During geomagnetically quiet times, overall, the PADs are quite similar at dawn and dusk. Only for 1 keV electrons, the PAD at dawn is slightly more anisotropic than that at dusk. Such dawn-dusk symmetry is expected from a quiet-time dawn-dusk symmetric geomagnetic field. The small differences in PADs at dawn and dusk for 1 keV electrons may be caused by quiet time convection electric field: though small, convection electric field still affects electron drift paths under quiet conditions, and such effects are more significant for lower-energy electrons than higher-energy electrons. Note that at $R = 4.5 R_E$, PADs of 30 keV electrons show some discrepancies at dawn and dusk during quiet times, which may be due to the relatively small number of samples at dawn.

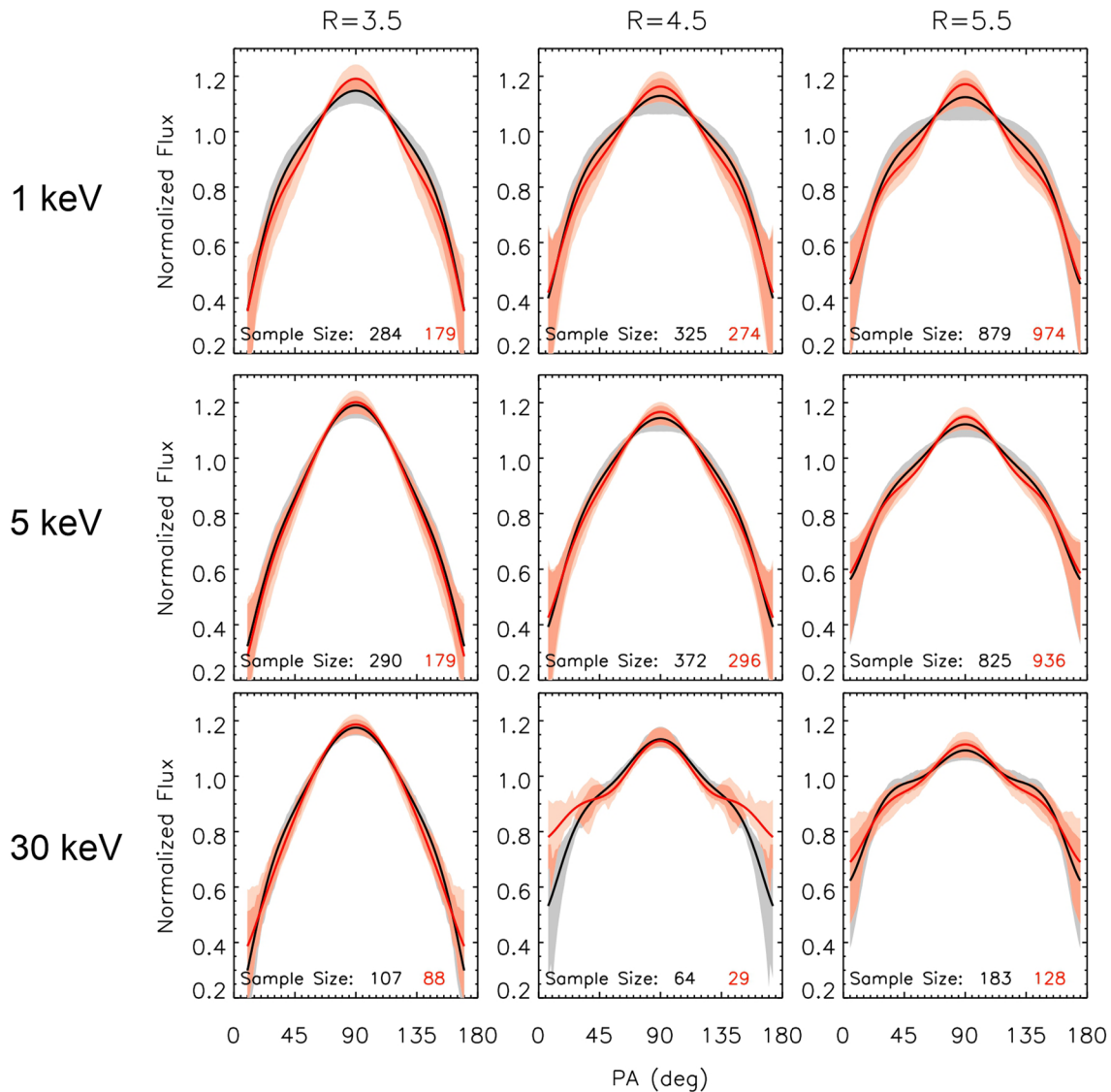


Figure 12. Comparison of averaged electron PADs at dawn (red) and dusk (black) under quiet geomagnetic activity. PAD, pitch angle distribution.

The situation becomes drastically different as the geomagnetic activity gets more intense. Figure 13 shows that for 1–10s of keV electrons, strong dawn-dusk asymmetry in PADs exists in a wide R range (~ 3.5 – 5.5), with much larger anisotropy in electron distribution at dawn than at dusk. These anisotropic electron distributions at dawn provide a significant energy source for the excitation of chorus waves, which are consistent with the observed enhanced chorus waves during active times near dawn by previous statistical studies (e.g., O. Agapitov et al., 2013; Aryan et al., 2014; W. Li et al., 2009; Meredith et al., 2012, 2003). The electron PAD model results further confirm the critical role of 1–10s of keV electrons in the excitation of chorus waves in the inner magnetosphere.

4. Summary

In this study, using ~ 7 years of data from the HOPE instrument on the Van Allen Probe—A, statistical analysis of 1–10s of keV electron equatorial PADs has been conducted, and an empirical model of electron equatorial PADs as a function of radial distance, magnetic local time, geomagnetic activity represented by the Kp index, and electron energy from 1 to 52 keV has been constructed. The main findings of this study include:

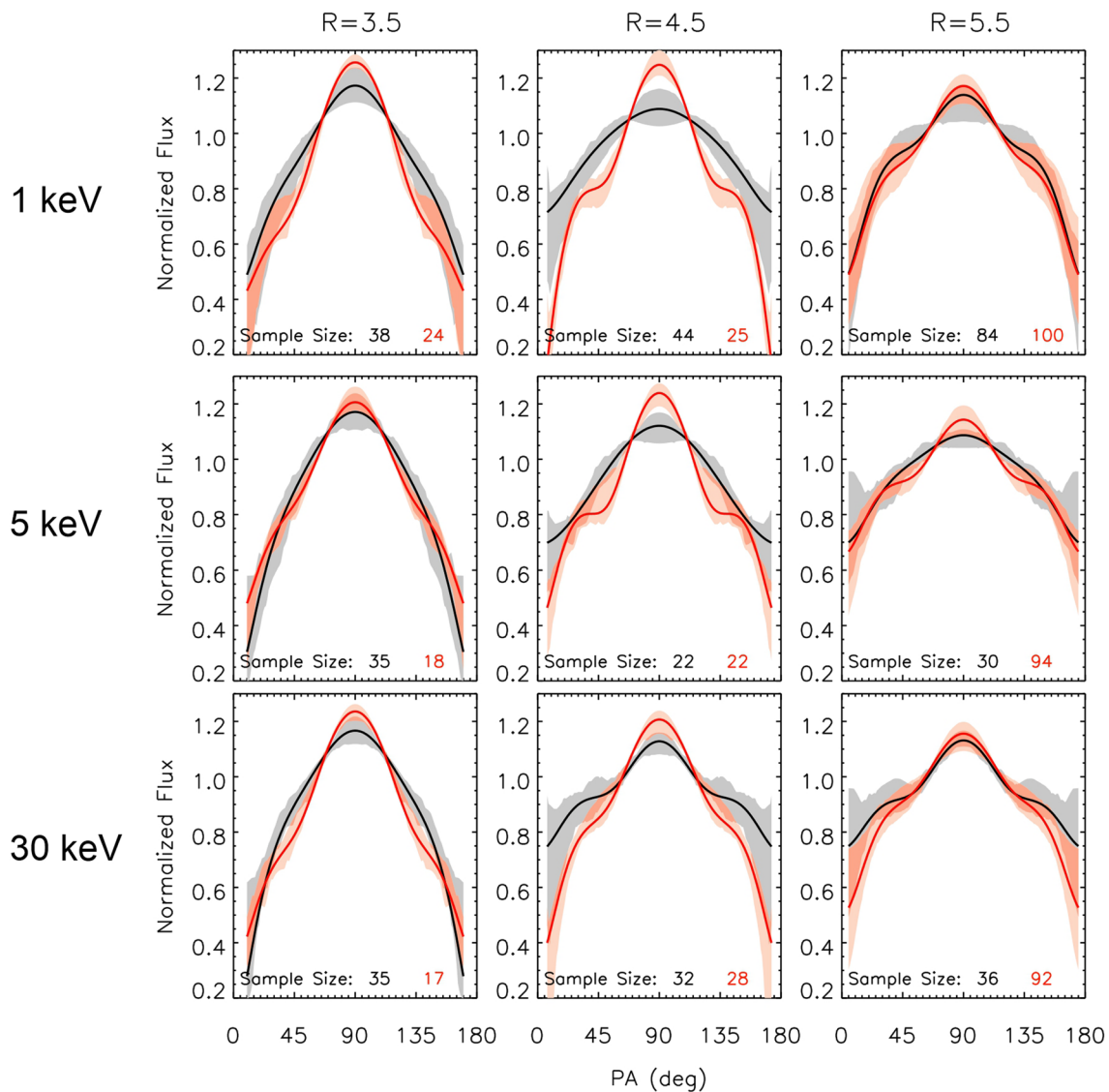


Figure 13. Similar format to Figure 11 but for active times.

1. Most equatorial PADs of 1–10s of keV electrons in Earth's inner magnetosphere are pancake PADs. This is very different from those of MeV electrons, which are often butterfly PADs at nightside. The lack of significant butterfly PADs of 1–10s of keV electrons is likely due to relatively flat or positive flux radial gradients of these electrons at higher altitudes
2. The anisotropy of 1–10s of keV electrons enhances significantly during geomagnetically active times, which is consistent with the enhanced chorus wave activity during active times, suggesting a critical role of these electrons in generating whistler-mode chorus waves in Earth's inner magnetosphere
3. Specific R- and MLT-dependent patterns of high anisotropy region of electrons with different energies exist during active times. More significant anisotropy of 1 keV electrons are observed at midnight to dawn at $R \sim 3\text{--}4 R_E$ and dawn to noon at $R > \sim 4 R_E$, while 5 and 30 keV electrons have larger anisotropy at midnight to dawn at $R > \sim 4 R_E$. These differences, combined with the statistical distribution of chorus waves as shown in previous studies, suggest the differential roles of electrons with different energies in generating chorus waves with different properties. Electrons with energies of 5–10s of keV could be mainly responsible for the generation of near-equatorial chorus waves, while the anisotropy of keV electrons could potentially lead to the generation of mid to high latitude highly oblique chorus waves

4. Day-night asymmetry in 1–10s of keV electron PADs at high R during geomagnetically quiet times is found, suggesting that the natural enhancement in electron anisotropy due to a stretched magnetic field could be responsible for the moderate chorus wave intensity at dayside during relatively quiet times. Such day-night asymmetry in electron anisotropy almost disappears for 5 and 30 keV electrons during active times, which may be related to energy-dependent drift caused by an enhanced electric field and/or more intense wave-particle interactions
5. Strong dawn-dusk asymmetry is observed for 1–10s of keV electron PADs during geomagnetically active times, with more anisotropic distributions near dawn than near dusk. These findings are consistent with the enhanced chorus wave intensity during active times, preferably around the dawn sector, further confirming the critical role of cyclotron resonance of 1–10s of keV electrons in the chorus wave excitation

Data Availability Statement

The parameters and sample programs of 1–50 keV electron pitch angle distribution model constructed in this study are available at <https://zenodo.org/record/3884260>. Van Allen Probes HOPE data are available at the ECT Science Operations and Data Center (<http://www.rbsp-ect.lanl.gov>). Kp index used in this study is available at OMNIWeb (<http://omniweb.gsfc.nasa.gov>).

Acknowledgment

This research was supported by RBSP-ECT funding through JHU/APL contract 967399 (under prime NASA contract NASS-01072).

References

- Agapitov, O., Artemyev, A., Krasnoselskikh, V., Khotyaintsev, Y. V., Mourenas, D., Breuillard, H., et al. (2013). Statistics of whistler-mode waves in the outer radiation belt: Cluster STAFF-SA measurements. *Journal of Geophysical Research: Space Physics*, *118*, 3407–3420. <https://doi.org/10.1002/jgra.50312>
- Agapitov, O. V., Artemyev, A. V., Mourenas, D., Mozer, F. S., & Krasnoselskikh, V. (2015). Empirical model of lower band chorus wave distribution in the outer radiation belt. *Journal of Geophysical Research: Space Physics*, *120*, 10425–10442. <https://doi.org/10.1002/2015JA021829>
- Aryan, H., Yearby, K., Balikhin, M., Agapitov, O., Krasnoselskikh, V., & Boynton, R. (2014). Statistical study of chorus wave distributions in the inner magnetosphere using Ae and solar wind parameters. *Journal of Geophysical Research: Space Physics*, *119*, 6131–6144. <https://doi.org/10.1002/2014JA019939>
- Baker, D. N., Higbie, P. R., Hones, E. W., Jr, & Belian, R. D. (1978). High-resolution energetic particle measurements at 6.6 RE 3. Low-energy electron anisotropies and short-term substorm predictions. *Journal of Geophysical Research*, *83*(A10), 4863–4868. <https://doi.org/10.1029/JA083iA10p04863>
- Baker, D. N., Hones, E. W., Jr, Higbie, P. R., & Belian, R. D. (1981). Global properties of the magnetosphere during a substorm growth phase: a case study. *Journal of Geophysical Research*, *86*(A11), 8941–8956.
- Bortnik, J., & Thorne, R. M. (2007). The dual role of ELF/VLF chorus waves in the acceleration and precipitation of radiation belt electrons. *Journal of Atmospheric and Solar-Terrestrial Physics*, *69*, 378–386. <https://doi.org/10.1016/j.jastp.2006.05.030>
- Boyd, A. J., Reeves, G. D., Spence, H. E., Funsten, H. O., Larsen, B. A., Skoug, R. M., et al. (2019). RBSP-ECT combined spin-averaged electron flux data product. *Journal of Geophysical Research: Space Physics*, *124*(11), 9124–9136. <https://doi.org/10.1029/2019JA026733>
- Burtis, W. J., & Helliwell, R. A. (1969). Banded chorus—A new type of VLF radiation observed in the magnetosphere by OGO 1 and OGO 3. *Journal of Geophysical Research*, *74*(11), 3002–3010. <https://doi.org/10.1029/JA074i011p03002>
- Califf, S., Li, X., Blum, L., Jaynes, A., Schiller, Q., Zhao, H., et al. (2014). THEMIS measurements of quasi-static electric fields in the inner magnetosphere. *Journal of Geophysical Research: Space Physics*, *119*, 9939–9951. <https://doi.org/10.1002/2014JA020360>
- Califf, S., Li, X., Zhao, H., Kellerman, A., Sarris, T. E., Jaynes, A., & Malaspina, D. M. (2017). The role of the convection electric field in filling the slot region between the inner and outer radiation belts. *Journal of Geophysical Research: Space Physics*, *122*, 2051–2068. <https://doi.org/10.1002/2016JA023657>
- Chen, Y., Friedel, R. H. W., Henderson, M. G., Claudepierre, S. G., Morley, S. K., & Spence, H. (2014). REPAD: An empirical model of pitch angle distributions for energetic electrons in the Earth's outer radiation belt. *Journal of Geophysical Research: Space Physics*, *119*, 1693–1708. <https://doi.org/10.1002/2013JA019431>
- Chen, Y., Reeves, G. D., Friedel, R. H. W., & Cunningham, G. S. (2014). Global time-dependent chorus maps from low-Earth-orbit electron precipitation and Van Allen Probes data. *Geophysical Research Letters*, *41*, 755–761. <https://doi.org/10.1002/2013GL059181>
- Funsten, H. O., Skoug, R. M., Guthrie, A. A., MacDonald, E. A., Baldonado, J. R., Harper, R. W., et al. (2013). Helium, oxygen, proton, and electron (HOPE) mass spectrometer for the Radiation Belt Storm Probes mission. *Space Science Reviews*, *179*, 423–484. <https://doi.org/10.1007/s11214-013-9968-7>
- Gannon, J. L., Li, X., & Heynderickx, D. (2007). Pitch angle distribution analysis of radiation belt electrons based on combined release and radiation effects satellite medium electrons A data. *Journal of Geophysical Research*, *112*, A05212. <https://doi.org/10.1029/2005JA011565>
- Hayakawa, M., Yamanaka, Y., Parrot, M., & Lefeuvre, F. (1984). The wave normals of magnetospheric chorus emissions observed on board GEOS 2. *Journal of Geophysical Research*, *89*(A5), 2811–2821. <https://doi.org/10.1029/JA089iA05p02811>
- Horne, R. B., Meredith, N. P., Thorne, R. M., Heynderickx, D., Iles, R. H. A., & Anderson, R. R. (2003). Evolution of energetic electron pitch angle distributions during storm time electron acceleration to megaelectronvolt energies. *Journal of Geophysical Research*, *108*(A1), 1016. <https://doi.org/10.1029/2001JA009165>
- Horne, R. B., Thorne, R. M., Glauert, S. A., Albert, J. M., Meredith, N. P., & Anderson, R. R. (2005). Timescale for radiation belt electron acceleration by whistler mode chorus waves. *Journal of Geophysical Research*, *110*, A03225. <https://doi.org/10.1029/2004JA010811>
- Kennel, C. F., & Petschek, H. E. (1966). Limit on stable trapped particle fluxes. *Journal of Geophysical Research*, *71*, 1–28. <https://doi.org/10.1029/JZ071i001p00001>

- Korth, H., Thomsen, M. F., Borovsky, J. E., & McComas, D. J. (1999). Plasma sheet access to geosynchronous orbit. *Journal of Geophysical Research*, *104*(A11), 25047–25061. <https://doi.org/10.1029/1999JA900292061>
- Li, W., Mourenas, D., Artemyev, A. V., Bortnik, J., Thorne, R. M., Kletzing, C. A., et al. (2016). Unraveling the excitation mechanisms of highly oblique lower band chorus waves. *Geophysical Research Letters*, *43*, 8867–8875. <https://doi.org/10.1002/2016GL070386>
- Li, J., Ni, B., Ma, Q., Xie, L., Pu, Z., Fu, S., et al. (2016). Formation of energetic electron butterfly distributions by magnetosonic waves via Landau resonance. *Geophysical Research Letters*, *43*, 3009–3016. <https://doi.org/10.1002/2016GL067853>
- Li, W., Ni, B., Thorne, R. M., Bortnik, J., Green, J. C., Kletzing, C. A., et al. (2013). Constructing the global distribution of chorus wave intensity using measurements of electrons by the POES satellites and waves by the Van Allen Probes. *Geophysical Research Letters*, *40*, 4526–4532. <https://doi.org/10.1002/grl.50920>
- Li, W., Thorne, R. M., Angelopoulos, V., Bortnik, J., Cully, C. M., Ni, B., et al. (2009). Global distribution of whistler-mode chorus waves observed on the THEMIS spacecraft. *Geophysical Research Letters*, *36*, L09104. <https://doi.org/10.1029/2009GL037595>
- Lyons, L. R., & Williams, D. J. (1975). The quiet time structure of energetic (35–560 keV) radiation belt electrons. *Journal of Geophysical Research*, *80*(7), 943–950. <https://doi.org/10.1029/JA080i007p00943>
- Mauk, B. H., Fox, N. J., Kanekal, S. G., Kessel, R. L., Sibeck, D. G., & Ukhorskiy, A. (2012). Science objectives and rationale for the radiation belt storm probes mission. *Space Science Reviews*, *179*, 1–15. <https://doi.org/10.1007/s11214-012-9908-y>
- Meredith, N. P., Horne, B., Sicard-Piet, A., Boscher, D., Yearby, K. H., Li, W., & Thorne, R. M. (2012). Global model of lower band and upper band chorus from multiple satellite observations. *Journal of Geophysical Research*, *117*, A10225. <https://doi.org/10.1029/2012JA017978>
- Meredith, N. P., Horne, R. B., Thorne, R. M., & Anderson, R. R. (2003). Favored regions for chorus-driven electron acceleration to relativistic energies in the Earth's outer radiation belt. *Geophysical Research Letters*, *30*(16), 1871. <https://doi.org/10.1029/2003GL017698>
- Ni, B., Zou, Z., Li, X., Bortnik, J., Xie, L., & Gu, X. (2016). Occurrence characteristics of outer zone relativistic electron butterfly distribution: A survey of Van Allen Probes REPT measurements. *Geophysical Research Letters*, *43*, 5644–5652. <https://doi.org/10.1002/2016GL069350>
- Reeves, G. D., Friedel, R. H. W., Larsen, B. A., Skoug, R. M., Funsten, H. O., Claudepierre, S. G., et al. (2016). Energy-dependent dynamics of keV to MeV electrons in the inner zone, outer zone, and slot regions. *Journal of Geophysical Research: Space Physics*, *121*, 397–412. <https://doi.org/10.1002/2015JA021569>
- Reeves, G. D., Spence, H. E., Henderson, M. G., Morley, S. K., Friedel, R. H. W., Funsten, H. O., et al. (2013). Electron acceleration in the heart of the Van Allen radiation belts. *Science*, *341*(6149), 991–994. <https://doi.org/10.1126/science.1237743>
- Santolik, O., Gurnett, D. A., Pickett, J. S., Chum, J., & Cornilleau-Wehrlin, N. (2009). Oblique propagation of whistler mode waves in the chorus source region. *Journal of Geophysical Research*, *114*, A00F03. <https://doi.org/10.1029/2009JA014586>
- Sarno-Smith, L. K., Larsen, B. A., Skoug, R. M., Liemohn, M. W., Breneman, A., Wygant, J. R., & Thomsen, M. F. (2016). Spacecraft surface charging within geosynchronous orbit observed by the Van Allen Probes. *Space Weather*, *14*, 151–164. <https://doi.org/10.1002/2015SW001345>
- Sarno-Smith, L. K., Liemohn, M. W., Skoug, R. M., Larsen, B. A., Moldwin, M. B., Katus, R. M., & Wygant, J. R. (2016). Local time variations of high-energy plasmaspheric ion pitch angle distributions. *Journal of Geophysical Research: Space Physics*, *121*, 6234–6244. <https://doi.org/10.1002/2015JA022301>
- Schulz, M., & Lanzerotti, L. (1974). *Particle diffusion in the radiation belts*. New York, NY: Springer. <https://doi.org/10.1007/978-3-642-65675-0>
- Selesnick, R. S., & Blake, J. B. (2002). Relativistic electron drift shell splitting. *Journal of Geophysical Research*, *107*(A9), 1265. <https://doi.org/10.1029/2001JA009179>
- Shi, R., Summers, D., Ni, B., Fennell, J. F., Blake, J. B., Spence, H. E., & Reeves, G. D. (2016). Survey of radiation belt energetic electron pitch angle distributions based on the Van Allen Probes MagEIS measurements. *Journal of Geophysical Research: Space Physics*, *121*, 1078–1090. <https://doi.org/10.1002/2015JA021724>
- Sibeck, D. G., McEntire, R. W., Lui, A. T. Y., Lopez, R. E., & Krimigis, S. M. (1987). Magnetic field drift shell splitting: Cause of unusual dayside particle pitch angle distributions during storms and substorms. *Journal of Geophysical Research*, *92*(A12), 13485–13497. <https://doi.org/10.1029/JA092iA12p13485>
- Spence, H. E., Reeves, G. D., Baker, D. N., Blake, J. B., Bolton, M., Bourdarie, S., et al. (2013). Science goals and overview of the energetic particle, composition, and thermal plasma (ECT) suite on NASA's radiation belt storm probes (RBSP) mission. *Space Science Reviews*. <https://doi.org/10.1007/s11214-013-0007-5>
- Thorne, R. M., Li, W., Ni, B., Ma, Q., Bortnik, J., Chen, L., et al. (2013). Rapid local acceleration of relativistic radiation belt electrons by magnetospheric chorus. *Nature*, *504*(7480), 411–414. <https://doi.org/10.1038/nature12889>
- Tsurutani, B. T., & Smith, E. J. (1977). Two types of magnetospheric ELF chorus and their substorm dependences. *Journal of Geophysical Research*, *82*(32), 5112–5128. <https://doi.org/10.1029/JA082i032p05112>
- Tsyganenko, N. A. (1989). A magnetospheric magnetic field model with a warped tail current sheet. *Planetary and Space Science*, *37*(1), 5–20. [https://doi.org/10.1016/0032-0633\(89\)90066-4](https://doi.org/10.1016/0032-0633(89)90066-4)
- Turner, D. L., Claudepierre, S. G., Fennell, J. F., O'Brien, T. P., Blake, J. B., Lemon, C., et al. (2015). Energetic electron injections deep into the inner magnetosphere associated with substorm activity. *Geophysical Research Letters*, *42*, 2079–2087. <https://doi.org/10.1002/2015GL063225>
- Wang, D., Shprits, Y. Y., Zhelavskaya, I. S., Agapitov, O. V., Drozdov, A. Y., & Aseev, N. A. (2019). Analytical chorus wave model derived from Van Allen Probe observations. *Journal of Geophysical Research: Space Physics*, *124*, 1063–1084. <https://doi.org/10.1029/2018JA026183>
- West, H. I. Jr., Buck, R. M., & Walton, J. R. (1973). Electron pitch angle distributions through the magnetosphere as observed on Ogo 5. *Journal of Geophysical Research*, *78*(7), 1064–1081. <https://doi.org/10.1029/JA078i007p01064>
- Yue, C., An, X., Bortnik, J., Ma, Q., Li, W., Thorne, R. M., et al. (2016). The relationship between the macroscopic state of electrons and the properties of chorus waves observed by the Van Allen Probes. *Geophysical Research Letters*, *43*, 7804–7812. <https://doi.org/10.1002/2016GL070084>
- Zhao, H., Baker, D. N., Califf, S., Li, X., Jaynes, A. N., Leonard, T., et al. (2017). Van Allen probes measurements of energetic particle deep penetration into the low L region ($L < 4$) during the storm on 8 April 2016. *Journal of Geophysical Research: Space Physics*, *122*, 12140–12152. <https://doi.org/10.1002/2017JA024558>
- Zhao, H., Friedel, R. H. W., Chen, Y., Reeves, G. D., Baker, D. N., Li, X., et al. (2018). An empirical model of radiation belt electron pitch angle distributions based on Van Allen Probes measurements. *Journal of Geophysical Research: Space Physics*, *123*, 3493–3511. <https://doi.org/10.1029/2018JA025277>
- Zhao, H., Li, X., Baker, D. N., Claudepierre, S. G., Fennell, J. F., Blake, J. B., et al. (2016). Ring current electron dynamics during geomagnetic storms based on the Van Allen Probes measurements. *Journal of Geophysical Research: Space Physics*, *121*, 3333–3346. <https://doi.org/10.1002/2016JA022358>

- Zhao, H., Li, X., Blake, J. B., Fennell, J. F., Claudepierre, S. G., Baker, D. N., et al. (2014a). Peculiar pitch angle distribution of relativistic electrons in the inner radiation belt and slot region. *Geophysical Research Letters*, *41*, 2250–2257. <https://doi.org/10.1002/2014GL059725>
- Zhao, H., Li, X., Blake, J. B., Fennell, J. F., Claudepierre, S. G., Baker, D. N., et al. (2014b). Characteristics of pitch angle distributions of hundreds of keV electrons in the slot region and inner radiation belt. *Journal of Geophysical Research: Space Physics*, *119*, 9543–9557. <https://doi.org/10.1002/2014JA020386>